Magnetization dynamics of elastically strained nanostructures studied by coupled micromagnetic-mechanical simulations

S. Chiroli,[1,*] D. Faurie,[1] M. Haboussi,[1] A. O. Adeyeye,[2,3] and F. Zighem[1]

[1]*LSPM - CNRS, UPR 3407, Université Sorbonne Paris Nord, 93430 Villetaneuse, France*

[2]*Department of Electrical and Computer Engineering, Information Storage Materials Laboratory, National University of Singapore, 117576 Singapore*

[3]*Department of Physics, Durham University, South Road, Durham DH1 3LE, United Kingdom*

(Received 3 April 2023; revised 8 June 2023; accepted 16 June 2023; published 10 July 2023)

Elastically strained ferromagnetic objects have been studied by coupled micromagnetic-mechanical numerical simulations. Both temporal evolution of the magnetization and modal frequency analysis of ferromagnetic thin films and arrays of nanostructures are presented. For this purpose, we have numerically coupled the micromagnetic equations (including magnetoelastic effects) to the ones of solid mechanics by including periodic boundary conditions. Our approach has been evaluated first on an elastically strained thin film and validated by performing *in situ* ferromagnetic resonance experiments. We have undertaken simulations on nanostructured arrays (modulated arrays of nanowires) and show that the heterogeneity of the strain fields and magnetic mode profiles of those strained nanostructures induce significative disparities in the magnetic mode energies, allowing applications to be foreseen where one could control in a differentiated way the spin-wave energies as a function of the applied elastic strains.

DOI: 10.1103/PhysRevB.108.024406

I. INTRODUCTION

Magnetoelastic effects in thin films and nanostructures have become a major field of research due to their fundamental aspects and for the industrial applications involving them [1–10]. Magnetoelastic effects are essentially those related to magnetostriction and which have the effect of either straining a ferromagnetic body under the application of a magnetic field (direct effect) or inducing a magnetoelastic anisotropy when a stress is applied to this body (indirect effect). Fundamental studies and applications related to these effects have been numerous during the last century (especially in the 1960s and '70s) but have been revived in recent years because they are more and more directly involved in various themes of nanomagnetism [11–14]. For instance, we have seen the emergence of what can be called "magnetic-straintronics," in which elastic (static) strains imposed on the system allow control of certain magnetic properties [2,5,9,10,15–17]. To this purpose we can associate an even more emerging theme—the curvilinear magnetism which allows highlighting complex magnetic textures in systems presenting strong curvatures [18–23]. The influence of these magnetoelastic effects is also very much studied in flexible magnetic systems which are generally composed of a magnetic deposit on a polymer substrate with applications ranging from everyday gadgets to aerospace devices [12,13]. *In operando*, these devices will be subjected to complex strain fields that can modify their magnetic properties [24,25]. For these systems, magnetoelasticity can be undesirable, and it is therefore necessary to find solutions to limit its effects. Therefore, despite numerous experimental studies, it is of utmost importance to develop numerical tools to describe heterogeneous strain and magnetoelastic fields in nano-objects. The numerical description of magnetic nanostructure behavior involves the resolution of the Landau-Lifshitz-Gilbert (LLG) equation. The commonly used softwares allow one to simulate the magnetic properties of nanostructures but are rarely used to take into account inhomogeneous strains. The magnetoelastic coupling must therefore be fully described at the scale of these inhomogeneities. Few groups have implemented numerical means that couple the LLG equation describing the magnetization dynamics as well as the solid mechanics ones in strain-mediated artificial multiferroics [26–31].

In this work we present a study describing the combined effects of shape and strain on nano-object magnetic response. Indeed, a complex-shaped object subjected to a macroscopic strain presents a nonuniform elastic and therefore magnetoelastic field distribution. These combined "shape-strain" effects must be well quantified, especially to interpret the experimental measurements. In this global context we present here a numerical approach to study the static and dynamic magnetic response of strained ferromagnetic thin films and nanostructures with different shape complexities. A particular focus is made on the energetic response of spin waves in magnetostrictive nano-objects, potentially affected by complex strain distribution. This approach has been first tested and validated thanks to experimental FMR measurements performed on thin films with and without magnetoelastic coupling and complex nanostructures that are presented later. We also simulate the evolution of magnetostatic modes of an array of width-modulated nanowires under an applied strain field in order to

*stephane.chiroli@univ-paris13.fr

highlight the benefits of elastic control of spin-wave features in such systems [32,33]. In this context, micromagnetic-micromechanical coupling is considered, which implies that one should be able to precisely calculate the strain field inside the magnetic medium, especially inside nanostructures where the strain field can be highly heterogeneous. For this purpose we choose to use COMSOL MULTIPHYSICS software based on the finite-element method [34]. This software has the advantage of allowing one to easily create complex geometries and couple multiple physics together, but no micromagnetic module exists.

II. METHODS

In this section we present the equations that we have solved, namely, the Landau-Lifshitz-Gilbert and mechanics equations. Thus we implemented the weak form of the following equations inside the software in order to use them for the finite-element method. Most of the theoretical considerations are described by Challab *et al.* in Ref. [31]. In the magnetic media, the temporal evolution of the reduced magnetization $\vec{m} = \frac{1}{M_s}(M_x\vec{e}_x + M_y\vec{e}_y + M_z\vec{e}_z)$, with M_s as the saturation magnetization, is governed by the LLG:

$$\frac{\partial \vec{m}(t)}{\partial t} = -\mu_0\gamma\vec{m}(t) \wedge \vec{H}_{\text{eff}} + \alpha\vec{m}(t) \wedge \frac{\partial \vec{m}(t)}{\partial t}, \tag{1}$$

where α is the Gilbert damping coefficient, and γ is the gyromagnetic ratio. By considering that the magnetization precession can be written $\vec{m}(t) = \vec{m}e^{i\omega t}$, where ω is the angular velocity of the spin precession, one can write Eq. (1) as follows:

$$i\omega(\vec{m} - \alpha\vec{m} \wedge \vec{m}) = -\mu_0\gamma\vec{m} \wedge \vec{H}_{\text{eff}}. \tag{2}$$

Equation (1) is therefore used to determine the equilibrium configuration of the magnetization, which is then used in Eq. (2) in order to perform a modal analysis. The magnetization dynamics is directly influenced by the effective magnetic field $\vec{H}_{eff} = -\frac{1}{\mu_{0M_s}}\frac{\delta F}{\delta \vec{m}}$, where F is the total magnetic energy of the system. This total energy can be written as the sum of the four energy terms we are considering in the context of this work: $F = F_{Zee} + F_{ex} + F_{ms} + F_{el}$, where the first term is the Zeeman energy density, the second one is the exchange [$F_{ex} = A(\nabla\vec{m})^2$] characterized by the exchange stiffness, and the third one is the magnetostatic energy density F_{ms} that depends on a demagnetizing field $\vec{H}_{\text{dem}}$ ($F_{ms} = -\frac{1}{2}\mu_0 M_s\vec{H}_{\text{dem}} \cdot \vec{m}$). $\vec{H}_{\text{dem}}$ is determined by introducing a magnetic potential ϕ such as $\mu_0\vec{H}_{\text{dem}} = -\vec{\nabla}\phi$. This potential is then calculated from the boundary conditions and is in most cases hard to analytically determine. Finally, the last energy term is the elastic energy, which exists in magnetostrictive materials and allows one to vary the magnetization by applying strain onto the material. Throughout this paper we only consider the magnetoelastic effects (indirect magnetostriction), because the direct magnetostriction is generally negligible compared to magnetoelastic effects. This elastic energy F_{el} can be written as

$$F_{el} = \tfrac{1}{2}\underline{\underline{\varepsilon^{el}}} : \underline{\underline{\underline{\underline{C}}}} : \underline{\underline{\varepsilon^{el}}}, \tag{3}$$

where $\underline{\underline{\varepsilon^{el}}}$ is the elastic strain, which can be expressed with the total strain and the magnetoelastic strain $\underline{\underline{\varepsilon^{el}}} = \underline{\underline{\varepsilon}} - \underline{\underline{\varepsilon^{m}}}$, with

$$\underline{\underline{\varepsilon}}(\vec{u}) = \frac{\vec{\nabla} \otimes \vec{u} + (\vec{\nabla} \otimes \vec{u})^T}{2}, \tag{4}$$

$$\underline{\underline{\varepsilon^{m}}} = \frac{3}{2}\lambda\begin{pmatrix} m_x^2 - \frac{1}{3} & m_x m_y & m_x m_z \\ m_x m_y & m_y^2 - \frac{1}{3} & m_y m_z \\ m_x m_z & m_y m_z & m_z^2 - \frac{1}{3} \end{pmatrix}. \tag{5}$$

In addition, as we are considering semi-infinite films or periodic array of nanostructures, we have applied periodic boundary conditions (PBCs) on the border of a single meshed unit cell, such as,

$$\vec{m}(\vec{r}) = \vec{m}(\vec{r} + \vec{a}), \tag{6}$$

$$\phi(\vec{r}) = \phi(\vec{r} + \vec{a}), \tag{7}$$

where $\vec{r}$ is the position vector, $\vec{a}$ is the translation to the next unit cell, and ϕ is the potential related to the demagnetizing field inside the magnetic material.

The use of these PBCs is illustrated in Fig. 1. These PBCs allow one to simulate a small portion of an infinite thin film, which considerably reduces the computing time. For instance, in Fig. 1(a), we calculate the equilibrium state of a chosen unit cell ($200 \times 200 \times 80$ nm^3) in the absence of elastic strain and at zero applied magnetic field. It should be emphasized that the automatic mesher of COMSOL was utilized to generate the mesh for the unit cells in the conducted simulations. Special attention has been given to the distance between two adjacent nodes so that it is of the same order of magnitude as the exchange length ($\ell_{ex} = \sqrt{\frac{2A}{\mu_0 M_S^2}}$). Furthermore, we have verified that for all the simulations presented in this article, a smaller size than this has no influence on the results obtained apart from elongating the computation time. Without the use of periodic boundary conditions (right image), the material behaves like a single square dot where the magnetic moment distribution presents a vortex configuration due to the shape of the object. In contrast, when PBCs are applied on the four faces of the (x, z) and (y, z) planes, we have been able to perfectly reproduce the behavior of a semi-infinite thin film of thickness 80 nm. Note that when PBCs are applied, it is easy to rotate the magnetization along the in-plane directions (as expected for a thin film with no in-plane anisotropy). This is illustrated in Fig. 1(b). A small magnetic field (10 mT) was applied in two different directions [along x and at 45° in the (x, y) plane], and we observe that the magnetic moment distribution at equilibrium is aligned along this applied field. However, it is very hard to saturate the magnetization along the out-of-plane direction due to the demagnetizing field, shown with the 500-mT and 1500-mT applied field along the z direction, illustrated in Fig. 1(c).

Sections B and C will focus on the magnetic response of periodic objects submitted to strain. Therefore it is also necessary to apply PBC for the displacement field as is done for the magnetization. However, since the strain is applied on multiple faces of the cell, it appears that some components of the strain field will be periodic whereas the others will be antiperiodic (an example is given in the

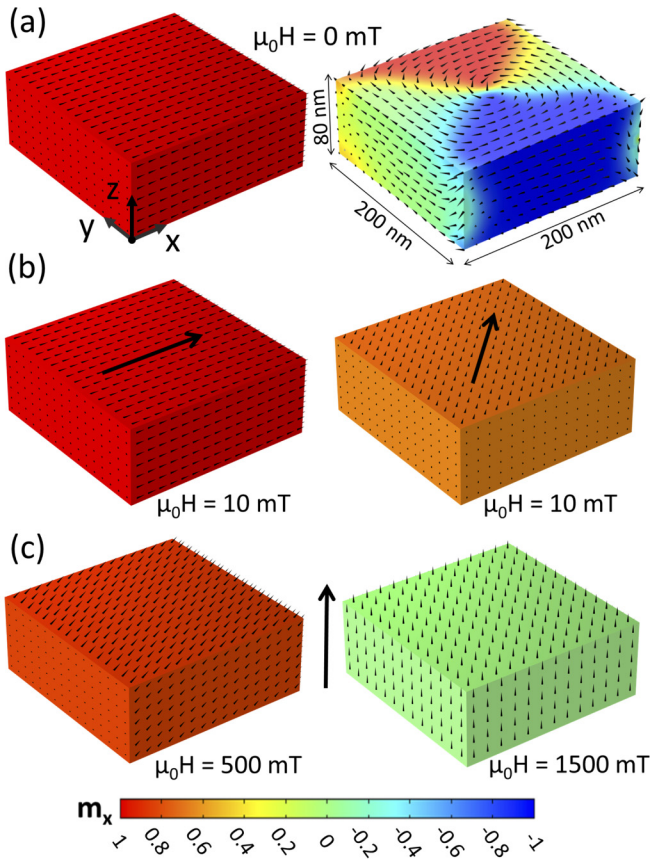

FIG. 1. In all images, colors encode the x component of the normalized magnetization from -1 to $+1$, see color bar. (a) Calculated magnetic moment distributions at zero applied magnetic field and at equilibrium for a unit cell $200 \times 200 \times 80$ nm^3 obtained with (left) or without (right) the defined periodic boundary conditions (PBCs). The PBCs have been applied at the four surfaces of the (x, z) and (y, z) planes. (b) Magnetic moment distributions calculated in presence of a 10-mT in-plane magnetic field applied either along x or at 45° with respect to the x axis. (c) Magnetic moment distribution calculated in presence of an out-of-plane magnetic field (500 mT and 1500 mT, respectively).

"Finite element method precisions" section of the Supplemental Material [35]).

III. RESULTS AND DISCUSSION

A. Broadband ferromagnetic resonance spectra of unstrained objects

Our approach was first used to simulate broadband ferromagnetic resonance experiments performed on thin films and nanostructures [36]. We conducted experiments to compare our numerical results with the experimental data. For this purpose, broadband ferromagnetic resonance (sweep-field FMR) experiments [37] have been conducted on an 80-nm $Ni_{80}Fe_{20}$ thin film deposited on a Si substrate. Two modes have been easily detected corresponding to the uniform precession mode and to the first perpendicular standing spin-wave one ($PSSW_1$). The study (see Supplemental Material [35]) of these two modes in different configurations (in-plane and out-of-plane measurements) allows the determination of the different magnetic parameters such as the effective magnetization $M_{\text{eff}} = 0.8 \times 10^6$ A m^{-1} (which is here equal to the saturation magnetization $M_s \sim M_{\text{eff}}$, since no out-of-plane anisotropy field has been detected), the gyromagnetic ratio $\gamma = 1.923 \times 10^{11}$ rad s^{-1} T^{-1}, and the exchange stiffness $A = 1.2 \times 10^{-11}$ J m^{-1}. These parameters were determined by using analytical formulas obtained under the macrospin assumptions [38]. Figure 2(a) presents the frequency of these two modes as function of an in-plane applied magnetic field (no in-plane anisotropy was detected for this film).

Our numerical approach was thus employed to simulate the variations of these two modes. We have first defined a representative elementary volume (a cuboid of dimensions $15 \times 15 \times 80$ nm^3) to which periodic boundary conditions have been applied (at four surfaces: (xz) and (yz) planes) in order to simulate an infinite thin film along the (xy) plane. The magnetic parameters used in the numerical simulations are those obtained experimentally by FMR. Before calculating the eigenfrequencies of the different modes, the equilibrium state (magnetic moment distribution) is first determined for a specific applied magnetic field. For this thin film, all the simulated equilibrium states correspond to a uniform distribution of the magnetic moments. These equilibrium states are then defined as a starting point for the frequency calculation, which is shown in Fig. 2(a).

The simulations of the frequency variation of the two modes show good agreement with the experimental data. The calculated uniform mode (green) follows almost perfectly the measured one, and the $PSSW_1$ is very close to the experimental one. It is to be noted that although the second-order perpendicular standing spin-wave ($PSSW_2$) mode was not experimentally detected, we have been able to simulate it [red symbols in Fig. 2(a)]. In the insets of Fig. 2(a), we have reported the calculated mode profiles for the uniform precession, the $PSSW_1$ and the $PSSW_2$ modes. The color map shows the power intensity, and it is interesting to note that, as expected, the uniform precession mode is uniform in thickness and along the (xy) plane. We also retrieve the well-known profiles of the $PSSW_1$ and $PSSW_2$, which reinforces the rigor of our approach regarding the calculation of mode energies and the extraction of their spatial profiles.

In order to further in the comparison of our approach with experiments, we have conducted FMR measurements on more complex objects. For this purpose, a 20-nm-thick $Ni_{80}Fe_{20}$ periodic array of width-modulated nanowires [32,33] deposited on Si has been studied. A scanning electron microscope image is presented as an inset in Fig. 2(b). One can note the width modulation of the nanowire, which makes this array more complex from a geometrical point of view. Thus the width is modulated so that the largest part is 230 nm wide and the thinnest part is 150 nm, while the periodicity of the array is around 600 nm (along y) and the modulation periodicity is 280 nm (along x). This modulation creates local inhomogeneities of the magnetization which creates several possibilities for the localized magnetic modes as compared to a uniform nanowire geometry.

FMR experiments were conducted in this array of width-modulated nanowires. Figure 2(b) presents typical spectra obtained for a magnetic field applied along the nanowires

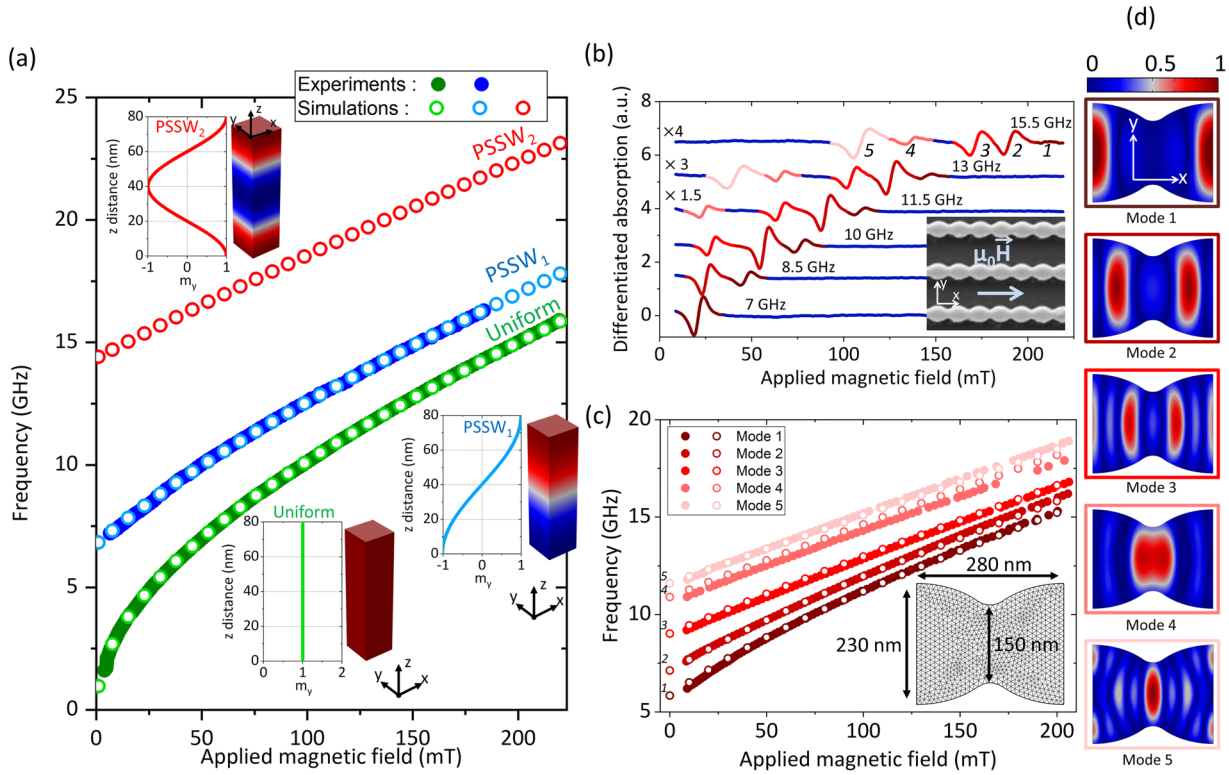

FIG. 2. (a) Experimental (filled symbols ●) and simulated frequency (open symbols ○) variations of the magnetostatic mode (uniform precession mode and perpendicular standing spin-wave modes) frequencies as a function of the magnetic field of a 80-nm-thick $Ni_{80}Fe_{20}$ film. The insets show 3D profiles of the different modes (colors encode the y component of the dynamic magnetization m_y), and a section along z is also represented next to each of these profiles (it was obtained in the center of the cell). (b) Typical sweep-field FMR spectrum recorded at a different driven frequency (from 7 to 15.5 GHz) in a 20-nm-thick $Ni_{80}Fe_{20}$ width-modulated array of nanowires with a magnetic field applied along the nanowires (along x direction). The inset shows a scanning electron microscopy image of this array: the periodicity of the array is 600 nm along y, while the width-modulation periodicity is 280 nm (larger width is 230 nm and the thinnest is 150 nm). (c) Experimental (filled symbols ●) and simulated frequency (open symbols ○) variations of the magnetostatic mode frequencies as a function of the magnetic field of array of nanowires. The inset shows a typical mesh of the representative elementary volume used for the simulations. (d) Top view of the calculated 3D magnetic mode profiles where colors encode m_y (see scale bar).

(along x) at multiple driven frequencies. One can clearly note the presence of at least five distinguishable magnetostatic modes of different amplitudes and of different linewidths. Similarly to the thin film, we have first defined a representative elementary volume which is presented as an inset in Fig. 2(c). The magnetic mode energies and their three-dimensional (3D) profiles have been then calculated. We have been able to identify the five experimental modes by comparing the numerical and experimental variations of their frequencies [see open symbols in Fig. 2(c)]. Typical extracted 3D modes are presented in Fig. 2(c). We found a good correlation between the experimental magnetic mode amplitudes and their calculated profiles—the larger the spin precession region, the larger the amplitude. This correlation is also valid for the experimental linewidth of the modes: the larger the region involved by the precession of the mode, the larger the experimental linewidth.

In the following sections (B and C) the magnetoelastic energy term is incorporated into the LLG finite-element resolution to account for the indirect magnetoelastic effect induced by the presence of external strain (see the Methods section for more details on the equations used).

B. Elastically strained thin film and magnetization dynamics response

The simplest application of magnetoelastic effects is the case of a continuous thin film subjected to strains from various sources (flexible substrate under tension or bending [39], ferroelectric substrate subjected to a voltage [40], effects of epitaxial interfaces [41], etc.). In this section we show how our numerical approach described allows to take into account these effects, whether they concern the static or the dynamic properties of the magnetization. More precisely, we have simulated a magnetoelectric system composed of a ferroelectric substrate on which a ferromagnetic thin film is deposited. The interest of this example is that we were able to confront the calculations to *in situ* FMR experiments (voltage applied to the substrate) [42]. The ferroelectric substrate is composed of polycrystalline PZT; more details can be found in Ref. [43]. Thus the imposed elastic strains by the substrate are transmitted to the thin film, which is itself magnetostrictive. Thus this study takes into account the magnetoelastic coupling in micromagnetic calculations. Here a macroscopic strain state is imposed on the edges of the substrate (along x and y),

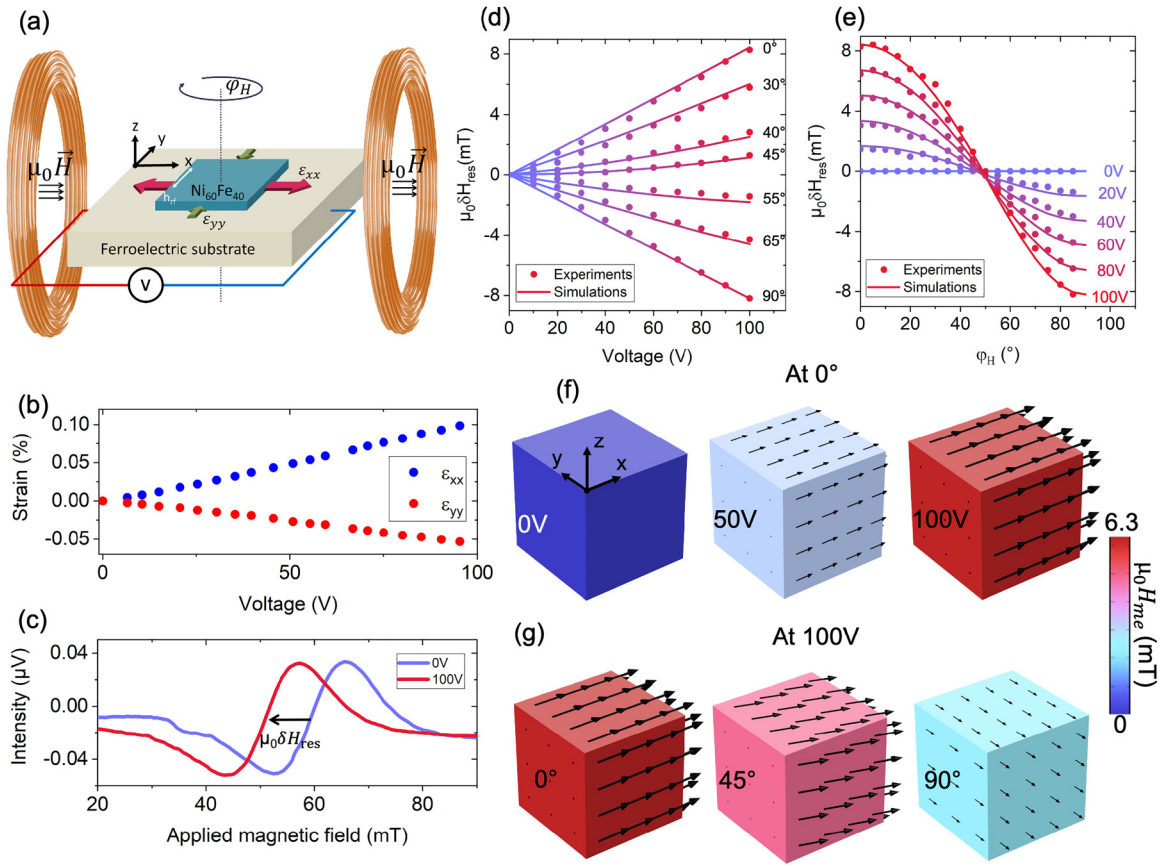

FIG. 3. (a) Schematic of $Ni_{60}Fe_{40}$ film/ferroelectric substrate system. $\mu_0\vec{H}$ corresponds to the applied magnetic field. (b) Ferroelectric substrate strain calibration curve. (c) FMR spectra obtained at 0 V (blue) and 100 V (red). (d) Resonance field shift [$\mu_0\delta H_{\rm res} = \mu_0 H_{\rm res}(0) - \mu_0 H_{\rm res}(V)$] as a function of the applied voltage. The experimental data are represented by symbols, while numerical results are represented by continuous lines. (e) Resonance field shift ($\mu_0\delta H_{\rm res}$) as a function of the in-plane φ_H. (f, g) Magnetoelastic field module map calculated for different values of the applied voltage at $\varphi_H = 0°$ (f) and for different angle at 100 V (g).

and its distribution (in this case homogeneous) is determined numerically.

Figure 3(a) shows a schematic of the studied system. A $Ni_{60}Fe_{40}$ thin film (20 nm) is deposited on a ferroelectric substrate whose $\varepsilon_{xx}(V)$ and $\varepsilon_{yy}(V)$ are experimentally known thanks to digital image correlation measurements; more details are given in Ref. [44]. ε_{xx} and ε_{yy} vary almost linearly between 0 and 100 V and respectively reach values of 1×10^{-3} and -0.5×10^{-3}; their evolutions are presented in Fig. 3(b). Indeed, ε_{xx} is found to be positive whereas ε_{yy} is found to be negative with a ratio $\varepsilon_{yy}/\varepsilon_{xx} \simeq -0.5$, making the mechanical traction slightly biaxial. These in-plane strains will then be injected in the micromagnetic simulations performed with a Young's modulus of $Y_{\rm N_{60}Fe_{40}} = 180$ GPa and a Poisson ratio $\nu = 0.3$. Figure 3(a) presents the sweep-field FMR experiments: a static magnetic field $\mu_0\vec{H}$ is applied in the plane of the film. The angle φ_H between $\mu_0\vec{H}$ and the main direction of traction (x) can vary from 0 to 90 degrees. On the schematic we have also represented the radio-frequency field (h_{rf}) imposed inside the film, which can excite the magnetic moments and thus probe the magnetostatic modes (here only the uniform mode is concerned). The complete study of the uniform precession mode by FMR allowed us to determine the magnetic parameters of the $Ni_{60}Fe_{40}$ thin film, namely, $M_s = 0.95 \times 10^6$ A m^{-1}, $A = 1.2 \times 10^{-11}$ J m^{-1}, and $\gamma = 1.76 \times 10^{11}$ rad s^{-1} T^{-1}. Those parameters will be used for the numerical simulations. Figure 3(c) shows typical experimental spectra at 8 GHz for two applied voltages (0 and 100 V). The magnetic field is applied along the main traction ($\varphi_H = 0°$) and the driven frequency is fixed at 8 GHz. We observe a shift of the resonance field $\mu_0\delta H_{\rm res} = \mu_0 H_{\rm res}(0) - \mu_0 H_{\rm res}(V)$ equal to $\sim +8$ mT. This shift is physically linked to the magnetoelastic field $\mu_0\vec{H}_{me}$ induced by the imposed in-plane strains from the substrate deformation. The positive sign of $\mu_0\delta H_{\rm res}$ allows us to deduce that the magnetostriction coefficient of the $Ni_{60}Fe_{40}$ film $\lambda_{\rm Ni_{60}Fe_{40}}$ is positive. Indeed, in this case $\mu_0\vec{H}_{me}$ is aligned along x, which decreases the resonance field (making x an easy axis). The complete experimental evolution (open symbols) of $\mu_0\delta H_{\rm res}$ as a function of V is shown in Fig. 3(d) for several φ_H angles. One can observe that $\mu_0\delta H_{\rm res} \sim -8$ mT for $\vec{H}$ applied at 90°, which is coherent with a uniaxial magnetoelastic field aligned along x. The complete in-plane variations of $\mu_0\delta H_{\rm res}$ are presented in Fig. 3(e) for several applied voltages. We recognize the signature of a second-order anisotropy axis, which is directly linked to the voltage-induced magnetoelastic anisotropy. It is clear that this magnetoelastic anisotropy is greater the more voltage is

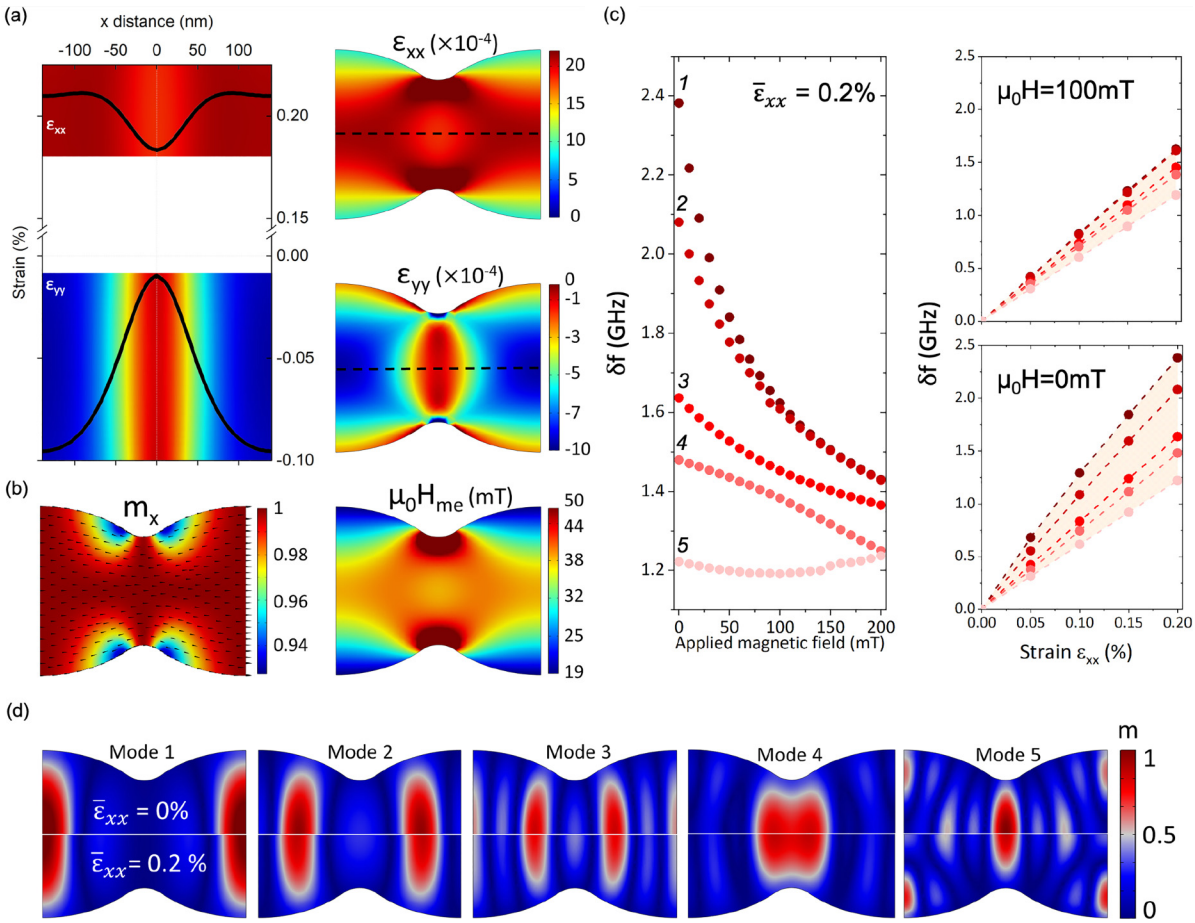

FIG. 4. (a) Top view of the spatial distribution of the induced in-plane strains ε_{xx} and ε_{yy} inside the nanowires for a macroscopic applied strain of $\bar{\varepsilon}_{xx} = 0.2\%$. Cross sections are shown on the right side of these strain maps, obtained from the black dotted lines on the mapping images. The colors correspond to a single pixel stretched along y and serve as a guide for the eyes. (b) Top view of the spatial distribution of the amplitude of the induced magnetoelastic field calculated in the absence of applied magnetic field ($\|\mu_0 \vec{H}_{me}\|$). The corresponding magnetic moment distribution is also represented. (c) Left graph: Frequency shift as function of the applied magnetic field; the frequency shift corresponds to the difference between the mode energies calculated at $\varepsilon_{xx} = 0.2\%$ and at $\varepsilon_{xx} = 0\%$. Right graphs: Frequency shift of the different magnetic modes as a function of ε_{xx} for an applied field of 100 mT along the nanowires (i.e., along x) and in the absence of applied field. (d) Top view of the spatial distribution of the magnetic modes calculated at $\varepsilon_{xx} = 0.2\%$ and at $\varepsilon_{xx} = 0\%$. The upper (resp. lower) section of each map has been computed with a strain of 0% (resp. 0.2%)

applied. The variations presented in Figs. 3(d) and 3(e) allow us to determine the magnetostriction coefficient for the thin film; by adjusting it, we found a value of $\lambda_{Ni_{60}Fe_{40}} \simeq +12 \times 10^{-6}$, as already found in Ref. [24].

Finally, we simulated the magnetomechanical behavior of this thin film subjected to homogeneous strains. For this purpose, a unit cell like the one presented in the previous section was used. The dimensions of the unit cell are $20 \times 20 \times 20$ nm^3. The PBC were applied on the four faces of the (x, z) and (y, z) planes to simulate a semi-infinite film in the (x, y) plane. We verified that our results remained unchanged by considering larger unit cells (along x and y). As expected, the application of PBC in the mechanic equations leads well to homogeneous induced strain fields in the film. The calculated induced magnetoelastic fields are also homogeneous for the different considered strain states. In this regard, Fig. 3(f) [resp. Fig. 3(g)] corresponds to the calculated induced static magnetoelastic field for different applied voltages [resp. in-plane angle φ_H] at $\varphi_H = 0°$ [resp. at 100 V] and at zero applied magnetic field. The colors encode the x component of the magnetoelastic field $\mu_0 H_{me}$ while the arrows show its distribution in the volume. In Fig. 3(f) we observe that the amplitude of $\mu_0 \vec{H}_{me}$ increases with the applied voltage, as shown by the arrow sizes on the 3D views. One can note that $\|\mu_0 \vec{H}_{me}\| \simeq 6.3$ mT at 100 V, which is different from the +8 mT found for $\mu_0 \delta H_{res}$ at 100 V. This is due to the slightly biaxial in-plane stress state induced by the ferroelectric substrate, due to the Poisson's ratio mismatch between substrate and thin film [44]. In addition, the same observation can be done in the images of Fig. 3(g). We notice that the $\mu_0 \vec{H}_{me}$ is weak but not zero at 90°, which would have been the case for a uniaxial stress state. We have indeed verified that when we impose a uniaxial stress state, the $\mu_0 \vec{H}_{me}$ cancels for $\varphi_H = 90°$. In order to compare our simulations more directly to the experimental results, we proceeded to calculations of eigenmodes as done in the previous section but in the presence of a mechanical stress in the film. So we added a magnetoelastic anisotropy term to the total energy density, which is dependent on the

mechanical stresses calculated in parallel with the resolution of the LLG equation. The magnetic parameters that have been used correspond to the values extracted from FMR experiments. Therefore we simulated several frequencies as a function of the applied magnetic field $f(H)$ curves by applying magnetic field varying from 0 to 250 mT (by steps of 10 mT) for different φ_H angles and at different mechanical stress states. We then numerically measured on the $f(H)$ curves the field shifts between these curves at a specific fixed frequency, which allows us to determine a shift similar to the one measured experimentally ($\mu_0\delta H_{\text{res}}$). We are thus in the same conditions as the *in situ* sweep-field FMR experiments. The continuous lines in Figs. 3(d) and 3(e) are thus the numerical $\mu_0\delta H_{\text{res}}$ variations. Note that no fit parameters were used. A very good agreement was found for both the $\mu_0\delta H_{\text{res}}$ variations at fixed φ_H [Fig. 3(d)] and at fixed applied voltage [Fig. 3(e)]. These results validate our approach, which combines mechanical calculations with the resolution of the LLG equation in the presence of a magnetoelastic term.

C. Differentiated elastic control of magnetic mode energies in a modulated array of nanowires

The previous case was characterized by a homogeneous strain field and thus is more simple to solve in terms of induced magnetoelastic field. However, in modern objects of nanomagnetism, the presence of strain gradients related to complex geometries requires a numerical modeling, taking into account the heterogeneous localization of the strains and thus the associated magnetoelastic field [45]. The approach developed here allows us to perform this kind of resolution and will be illustrated in this section by the numerical study of the magnetomechanical properties of modulated nanowires already discussed.

For this study we employed the same magnetic parameters as presented in Fig. 1(c). Since $Ni_{80}Fe_{20}$ is nonmagnetostrictive, we opted to use a magnetoelastic constant λ of 30×10^{-6}, which is typical for ferromagnetic polycrystalline thin films. Additionally, we utilized a Young's modulus Y of 180 GPa and a Poisson ratio ν of 0.3 for the purpose of this study. These chosen parameters provide a reasonable approximation for the magnetoelastic behavior in the absence of direct experimental measurements.

Modulated nanowires were numerically submitted to external strains along their main axis (x). PBCs were adopted so that the representative unit cell [identical to that used in Fig. 2(c)] allows the determination of the whole behavior. Different external strains were applied (from 0% to 0.2% with 0.05% step). Figure 4(a) shows the in-plane strain (ε_{xx}, ε_{yy}) maps at the top surface of the unit cell (right images) for a macroscopic applied strain of $\overline{\varepsilon}_{xx} = 0.2\%$. We observe that the strain fields are heterogeneous in the (x, y) plane but homogeneous over the thickness. This is due to the width modulation of the nanowires; indeed, nanowires without modulation would have presented much more homogeneous strain fields. These inhomogeneities are illustrated on the left graph where we have represented a cut along the nanowire (dashed line in the maps). It is interesting to note that the variations of ε_{xx} and ε_{yy} are respectively located at around $+0.2$ and -0.06, which correspond to the macroscopic values of $\overline{\varepsilon}_{xx}$ and $\overline{\varepsilon}_{yy}$.

These heterogeneous values naturally give rise to a heterogeneous magnetoelastic field. This is illustrated in Fig. 4(b), where the amplitude of $\mu_0\vec{H}_{me}$ has been calculated from the strain fields presented in Fig. 4(a) and the equilibrium magnetization distribution [see left map of Fig. 4(b)] obtained in the absence of the applied magnetic field for a macroscopic strain of $\overline{\varepsilon}_{xx} = 0.2\%$. It should be mentioned that H_{me} and the magnetization distribution are obtained in a self-consistent scheme. This magnetoelastic field configuration is thus directly linked to the strain-field configuration and, more particularly, to that of ε_{xx} since the magnetic moments are mostly oriented in the x direction. We have followed the evolution of the frequencies of the different magnetic modes identified in the previous section at different macroscopic strain values. Figure 4(c) (left graph) shows the frequency shift $[\delta f = f(0) - f(\overline{\varepsilon}_{xx})]$ obtained for an applied macroscopic strain of 0.2% for increasing applied magnetic field. It is interesting to note that not all modes show the same frequency shift for a given magnetic field. Moreover, the lower frequency modes have the largest δf. For instance, at zero applied field, mode 1 has a frequency shift of $\delta f \sim 2.4$ GHz, while it is twice as low for mode 5 ($\delta f \sim 1.2$ GHz). These lowest frequency modes' δf are also the most affected by the applied magnetic field. In order to emphasize this phenomenon, we plotted the δf evolution of each mode with respect to the applied macroscopic strain at 0 and 100 mT. In Fig. 4(c) (right graphs) we observe an almost linear dependency of the modes to the applied strain, which has been experimentally observed in the elastic regime in saturated magnetic configurations [24]. These graphs show that the lowest frequency modes are getting closer to the higher modes' behavior as the magnetic field increases, which can be related to the experimental and numerical data shown in Fig. 2(c). Indeed, we observe in this figure that the mode evolution slopes are different for each mode at low magnetic field, which gives birth to a differentiated mode control with the applied strain. As the applied field increases, the slopes tend to equalize, which explains the tightening evolution of all the modes as function of $\overline{\varepsilon}_{xx}$. To understand the observation of such a difference at low applied field, we scrutinized the spatial distribution of each of the magnetic modes at minimum ($\overline{\varepsilon}_{xx} = 0\%$) and maximum applied strain ($\overline{\varepsilon}_{xx} = 0.2\%$). The different spatial distributions of the five modes are presented in Fig. 4(d); the upper (resp. lower) half corresponds to maps obtained at a strain of 0% (resp. 0.2%). It is interesting to notice that the lowest frequency modes (especially modes 1 and 2) show a clear variation of their spatial distribution, whereas the higher frequency modes remain mainly in the same spatial region. This is most probably related to the progressive saturation of the magnetization close to the borders of the modulated nanowires and would explain why at high applied field the lowest frequency modes δf are highly reduced. These mode frequency shifts are only observable thanks to the coupling between the LLG and the equations of mechanics in the case of magnetostrictive materials. In the case an infinite non magnetostrictive material ($\lambda = 0$), no shift is observed numerically; however, in the case of the modulated nanowire array a very small shift (negligible compared to the magnetoelastic effect) is observed due to the slight shape modification induced by the strain.

IV. CONCLUSION

In this paper, the Landau-Lifshitz-Gilbert equation as well as Maxwell's equations have been implemented and solved under COMSOL MULTIPHYSICSby coupling them with the equations of solid mechanics to take into account magnetoelastic effects. Moreover, the introduction of periodic boundary conditions allowed us to simulate the magnetization dynamics of elastically strained thin films and arrays of nanostructures. We were able to simulate precisely the uniform mode behavior of an elastically strained $Ni_{60}Fe_{40}$ thin film (with a slightly biaxial stress) through a ferroelectric actuator. Specifically, we were able to account for the voltage-induced strain magnetoelastic anisotropy by performing measurements and simulations for different values of the angle between the applied field and the principal axis of the applied stress. Finally, the study conducted on modulated nanowires revealed a differentiation in the elastic control of the spin-wave modes which is partly due to the heterogeneity of the strain-induced magnetoelastic field. This approach is very promising to develop multichannel systems with simultaneous and differentiated controlled frequencies in magnetic devices.

A direct extension of this work would be to consider dispersive effects (spin waves) to simulate the propagation of spin waves. The approach we have developed is well suited to tackle this by modifying the periodic boundary conditions through phase shifts applied to different faces of our system, effectively simulating a wave vector. This extension can be used to simulate spin-wave propagation not only in semi-infinite layers but also in arrays of nanostructures such as magnonic crystals. In these arrays, spin-wave band structures can emerge due to the confinement of spin waves and their propagation through the crystal. Moreover, dynamic direct magnetostrictive effects can be judiciously implemented to account for potential dynamic interactions with acoustic waves. It is indeed possible to study the properties of so-called "magphonics" crystals, which exhibit both phononic and magnonic characteristics, by simulating their magnon and phonon band structures along with their interactions (due to direct magnetostriction) [46,47].

ACKNOWLEDGMENTS

This work was supported by the French-Singaporean International Research Program (IRP CNRS-NUS Stretch-Smart) within the framework of the ElecAcouSpin ANR project, Grant No. ANR-19-CE24-0009, of the French Agence Nationale de la Recherche (ANR). The authors want to thank Nicolas Greneche, responsible for the MAGI server in USPN, and Dr. Nabil Challab, for his support during the simulations.

[1] G. S. Cañón Bermúdez and D. Makarov, Adv. Funct. Mater. **31**, 2007788 (2021).
[2] C. L. Chang, S. Mieszcak, M. Zelent, V. Besse, U. Martens, R. R. Tamming, J. Janusonis, P. Graczyk, M. Münzenberg, J. W. Kłos, and R. I. Tobey, Phys. Rev. Appl. **10**, 064051 (2018)
[3] A. Bedoya-Pinto, M. Donolato, M. Gobbi, L. E. Hueso, and P. Vavassori, Appl. Phys. Lett. **104**, 062412 (2014).
[4] M. Kondo, M. Melzer, D. Karnaushenko, T. Uemura, S. Yoshimoto, M. Akiyama, Y. Noda, O. G. Schmidt, and T. Sekitani, Sci. Adv. **6**, eaay6094 (2020).
[5] A. V. Azovtsev and N. A. Pertsev, Phys. Rev. B **94**, 184401 (2016).
[6] M. Ha, G. S. Cañón Bermúdez, T. Kosub, I. Mönch, Y. Zabila, E. S. Oliveros Mata, R. Illing, Y. Wang, J. Fassbender, and D. Makarov, Adv. Mater. **33**, 2005521 (2021).
[7] S. Zhao, Z. Zhou, C. Li, B. Peng, Z. Hu, and M. Liu, ACS Nano **12**, 7167 (2018).
[8] L. Shen, G. Lan, L. Lu, C. Ma, C. Cao, C. Jiang, H. Fu, C. You, X. Lu, Y. Yanf, L. Chen, M. Liu, and C. L. Jia, Adv. Sci. **5**, 1800855 (2018).
[9] M. Jaris, W. Yang, C. Berk, and H. Schmidt, Phys. Rev. B **101**, 214421 (2020)
[10] A. C. Chavez, J. D. Schneider, A. Barra, S. Tiwari, R. N. Candler, and G. P. Carman, Phys. Rev. Appl. **12**, 044071 (2019)
[11] D. Makarov, M. Melzer, D. Karnaushenko, and O. G. Schmidt, Appl. Phys. Rev. **3**, 011101 (2016).
[12] M. Melzer, D. Makarov, and O. G. Schmidt, J. Phys. D: Appl. Phys. **53**, 083002 (2019).
[13] F. Zighem and D. Faurie, J. Phys.: Condens. Matter **33**, 233002 (2021).
[14] D. Faurie, A. O. Adeyeye, and F. Zighem, J. Appl. Phys. **130**, 150901 (2021).
[15] A. K. Biswas, J. Atulasimha, and S. Bandyopadhyay, Nanotechnology **26**, 285201 (2015).
[16] M. Buzzi, R. V. Chopdekar, J. L. Hockel, A. Bur, T. Wu, N. Pilet, P. Warnicke, G. P. Carman, L. J. Heyderman, and F. Nolting, Phys. Rev. Lett. **111**, 027204 (2013).
[17] X. Liang, C. Dong, H. Chen, J. Wang, Y. Wei, M. Zaeimbashi, Y. He, A. Matyushov, C. Sun, and N. Sun, Sensors **20**, 1532 (2020).
[18] D. Makarov and D. D. Sheka, *Curvilinear Micromagnetism: From Fundamentals to Applications, Topics in Applied Physics* (Springer, New York, 2022).
[19] K. V. Yershov and D. D. Sheka, Phys. Rev. B **107**, L100415 (2023).
[20] D. Raftrey, A. Hierro-Rodriguez, A. Fernandez-Pacheco, and P. Fischer, J. Magn. Magn. Mater. **563**, 169899 (2022).
[21] D. Makarov, O. M. Volkov, A. Kákay, O. V. Pylypovskyi, B. Budinská, and O. V. Dobrovolskiy, Adv. Mater. **34**, 2101758 (2022).
[22] D. D. Sheka, O. V. Pylypovskyi, P. Landeros, Y. Gaididei, A. Kákay, and D. Makarov, Commun. Phys. **3**, 128 (2020).
[23] P. Makushko, T. Kosub, O. V. Pylypovskyi, N. Hedrich, J. Li, A. Pashkin, S. Avdoshenko, R. Hübner, F. Ganss, D. Wolf *et al.*, Nat. Commun. **13**, 6745 (2022).
[24] N. Challab, D. Faurie, M. Haboussi, A. O. Adeyeye, and F. Zighem, ACS Appl. Mater. Interfaces **13**, 29906 (2021).
[25] N. Challab, F. Zighem, D. Faurie, M. Haboussi, M. Belmeguenai, P. Lupo, and A. O. Adeyeye, Phys. Status Solidi RRL **13**, 1800509 (2019).
[26] C. Y. Liang, S. M. Keller, A. E. Sepulveda, A. Bur, W. Y. Sun, K. Wetzlar, and G. P. Carman, Nanotechnology **25**, 435701 (2014).

[27] C. Y. Liang, S. M. Keller, A. E. Sepulveda, W. Y. Sun, J. Cui, C. S. Lynch, and G. P. Carman, J. Appl. Phys. **116**, 123909 (2014).
[28] Z. Xiao, R. Lo Conte, C. Chen, C. Y. Liang, A. Sepulveda, J. Bokor, G. P. Carman, and R. N. Candler, Sci. Rep. **8**, 5207 (2018).
[29] N. K. P. Babu, A. Trzaskowska, P. Graczyk, G. Centała, S. Mieszczak, H. Głowiński, M. Zdunek, S. Mielcarek, and J. W. Kłos, Nano Lett. **21**, 946 (2020).
[30] D. Froes, M. Arana, J. P. Sinnecker, and L. C. Sampaio, J. Appl. Phys. **132**, 223908 (2022).
[31] N. Challab, A. D. Aboumassound, F. Zighem, D. Faurie, and Haboussi, J. Phys. D: Appl. Phys. **52**, 355004 (2019).
[32] L. L. Xiong and A. O. Adeyeye, Appl. Phys. Lett. **108**, 262401 (2016).
[33] L. L. Xiong, M. Kostylev, and A. O. Adeyeye, Phys. Rev. B **95**, 224426 (2017).
[34] COMSOL Multiphysics® v. 6.1. www.comsol.com. COMSOL AB, Stockholm, Sweden.
[35] Please see the Supplemental Material at http://link.aps.org/supplemental/10.1103/PhysRevB.108.024406 for technical details on the experimental characterization of thin films by ferromagnetic resonance as well as details on numerical simulations, particularly with regard to the periodic boundary conditions described in the text.
[36] J. Ding, M. Kostylev, and A. O. Adeyeye, Phys. Rev. B **84**, 054425 (2011).
[37] F. Zighem, D. Faurie, M. Belmeguenai, A. Garcia-Sanchez, P. Lupo, and A. O. Adeyeye, Appl. Phys. Lett. **111**, 052408 (2017).
[38] C. Kittel, Phys. Rev. **73**, 155 (1948).
[39] M. Gueye, B. M. Wague, F. Zighem, M. Belmeguenai, M. S. Gabor, Jr., T. Petrisor, C. Tiusan, S. Mercone, and D. Faurie, Appl. Phys. Lett. **105**, 062409 (2014)
[40] M. Gueye, F. Zighem, D. Faurie, M. Belmeguenai, and S. Mercone, Appl. Phys. Lett. **105**, 052411 (2014)
[41] S. Goel, L. D. Anh, S. Ohya, and M. Tanaka, Phys. Rev. B **99**, 014431 (2019).
[42] M. Gueye, P. Lupo, F. Zighem, D. Faurie, M. Belmeguenai, and A. O. Adeyeye, Europhys. Lett. **114**, 17003 (2016).
[43] T. Sadat, D. Faurie, P. Godard, D. Thiaudière, P.-O. Renault, and F. Zighem, J. Phys. D: Appl. Phys. **53**, 145001 (2020)
[44] F. Zighem, M. Belmeguenai, D. Faurie, H. Haddadi, and J. Moulin, Rev. Sci. Instrum. **85**, 103905 (2014)
[45] N. Challab, D. Faurie, M. Haboussi, and F. Zighem, Phys. Status Solidi RRL **15**, 2100149 (2021)
[46] P. Graczyk and M. Krawczyk, Phys. Rev. B **96**, 024407 (2017)
[47] V. L. Zhang, F. S. Ma, H. H. Pan, C. S. Lin, H. S. Lim, S. C. Ng, M. H. Kuok, S. Jain, and A. O. Adeyeye, Appl. Phys. Lett. **100**, 163118 (2012).